

TURBULENCE IN THE OUTER REGIONS OF PROTOPLANETARY DISKS.
I. WEAK ACCRETION WITH NO VERTICAL MAGNETIC FLUXJACOB B. SIMON¹, XUE-NING BAI^{2,3,4}, JAMES M. STONE², PHILIP J. ARMITAGE^{1,5}, AND KRIS BECKWITH^{1,6}*Draft version October 16, 2018*

ABSTRACT

We use local numerical simulations to investigate the strength and nature of magnetohydrodynamic (MHD) turbulence in the outer regions of protoplanetary disks, where ambipolar diffusion is the dominant non-ideal MHD effect. The simulations include vertical stratification and assume zero net vertical magnetic flux. We employ a super time-stepping technique to ameliorate the Courant restriction on the diffusive time step. We find that in idealized stratified simulations, with a spatially constant ambipolar Elsasser number Am , turbulence driven by the magnetorotational instability (MRI) behaves in a similar manner as in prior unstratified calculations. Turbulence dies away for $Am \leq 1$, and becomes progressively more vigorous as ambipolar diffusion is decreased. Near-ideal MHD behavior is recovered for $Am \geq 10^3$. In the intermediate regime ($10 \leq Am \leq 10^3$) ambipolar diffusion leads to substantial increases in both the period of the MRI dynamo cycle and the characteristic scales of magnetic field structures. To quantify the impact of ambipolar physics on disk accretion, we run simulations at 30 AU and 100 AU that include a vertical Am profile based upon far ultraviolet (FUV) ionized disk models. These models develop a vertically layered structure analogous to the Ohmic dead zone that is present at smaller radii. We find that, although the levels of surface turbulence can be strong (and consistent with constraints on turbulent line widths at these radii), the inferred accretion rates are at least an order of magnitude smaller than those observed in T Tauri stars. This discrepancy is very likely due to the assumption of zero vertical magnetic field in our simulations and suggests that vertical magnetic fields are essential for MRI-driven accretion in the outer regions of protoplanetary disks.

Subject headings: accretion, accretion disks — (magnetohydrodynamics:) MHD — turbulence — protoplanetary disks

1. INTRODUCTION

The structure and evolution of protoplanetary disks play a crucial role in the formation of stars and their planetary systems. Disk gas is observed to accrete onto the central star at rates that require some form of angular momentum transport substantially stronger than that provided by molecular viscosity. Turbulence has long been suggested as the source of enhanced transport (Shakura & Syunyaev 1973). This turbulence not only allows for accretion, but can also play an important role in the formation and subsequent evolution of planets. At early times, turbulence can act to inhibit dust settling and largely determine the collisional velocities that affect the balance between fragmentation and coagulation of these particles (Ormel & Cuzzi 2007; Youdin & Lithwick 2007; Birnstiel et al. 2011). Persistent pressure maxima predicted by some turbulence models (Barge & Sommeria 1995; Johansen et al. 2009; Uribe et al. 2011; Simon et al. 2012) may act to concentrate particles, enhancing their coagulation into larger

particles. Once planetesimals have formed, gravitational coupling to turbulent fluctuations in the disk may affect their growth (Ida et al. 2008). Finally, the strength and nature of turbulence determines whether the critical co-orbital contribution to the Type I migration torque remains unsaturated (Paardekooper et al. 2011).

At a minimum, turbulence in protoplanetary disks will be generated in regions where the magnetorotational instability (MRI; Balbus & Hawley 1998) operates. Indeed, simulations of the non-linear evolution of the MRI under ideal magnetohydrodynamic (MHD) conditions yield sustained turbulence that transports angular momentum outward at rates in general agreement with observations (Hartmann et al. 1998). However, large regions of protoplanetary disks are expected to have very low ionization fractions (e.g., Ilgner & Nelson 2006), which in turn result in three significant non-ideal MHD effects: Ohmic diffusion, ambipolar diffusion, and the Hall effect (see, e.g., Armitage 2011). The relative importance of these effects depends primarily upon the density (as well as magnetic field strength). Ohmic diffusion is efficient at high densities, and is thus most important in the inner regions of the disk (outside a small zone very close to the star where thermal ionization of alkali metals provides sufficient ionization throughout the disk column). At low gas densities, such as in the outer disk, ambipolar diffusion becomes dominant, while at intermediate densities, the Hall term is important (e.g., Kunz & Balbus 2004).

MRI physics and the phenomenological consequences

jbsimon@jila.colorado.edu

¹ JILA, University of Colorado and NIST, 440 UCB, Boulder, CO 80309-0440² Department of Astrophysical Sciences, Princeton University, Princeton, NJ 08544³ Hubble Fellow⁴ Current address: Harvard-Smithsonian Center for Astrophysics, 60 Garden St., MS-51, Cambridge, MA 02138⁵ Department of Astrophysical and Planetary Sciences, University of Colorado, Boulder, CO 80309⁶ Tech-X Corporation, 5621 Arapahoe Ave., Suite A, Boulder, CO 80303

of the non-ideal terms have been best-characterized in the case of Ohmic diffusion. The evolution in this limit depends upon the Elsasser number, defined as $\Lambda \equiv v_{A,z}^2/\eta\Omega$, where $v_{A,z}$ is the Alfvén velocity in the vertical direction, η is the Ohmic resistivity, and Ω is the angular frequency of Keplerian rotation. For Λ less than order unity, MRI turbulence is severely quenched (Jin 1996; Turner et al. 2007), while for larger values the MRI saturation level will depend on the strength of Ohmic diffusion; stronger diffusion leads to lower turbulence levels. Combining these results with chemical models for disks motivates the dead zone model of disk accretion (Gammie 1996). In this model, the disk is well-ionized only in its surface layers due to non-thermal sources (X-rays, cosmic rays, and far ultraviolet (FUV) photons) that penetrate the disk from the exterior down to some column depth. Closer to the mid-plane, the ionization fraction is low, resulting in a small Λ , and no MRI-driven turbulence (e.g., Gammie 1996; Fleming & Stone 2003; Turner et al. 2007; Turner & Sano 2008; Oishi & Low 2009). Thus, MRI-driven accretion occurs in active layers only, leaving much of the disk mass near the mid-plane magnetically inactive.

Qualitative changes to the predicted disk structure may equally result from ambipolar diffusion and the Hall effect, though for these terms the understanding of the non-linear behavior is incomplete. The *linear* regime of the MRI in the presence of the Hall term has been explored by Wardle (1999), Balbus & Terquem (2001), and Wardle & Salmeron (2012). A primary result from these studies is that the growth rate of the MRI is strongly affected by the sign of $\boldsymbol{\Omega} \cdot \mathbf{B}$, i.e., how the vertical magnetic field is aligned with the angular velocity vector. The only study of the non-linear, turbulent state of the MRI in the presence of the Hall term was carried out in Sano & Stone (2002a) and Sano & Stone (2002b). Their numerical simulations included both Ohmic diffusion *and* the Hall term, with the Ohmic contribution dominating significantly over the Hall effect. In this regime, the Hall term does not strongly influence the saturated state of the MRI. However, the regime in which the Hall term dominates has yet to be explored through simulations (Wardle & Salmeron 2012).

Ambipolar diffusion arises from the imperfect coupling between ionized species and neutrals. The linear analyses of Blaes & Balbus (1994), Kunz & Balbus (2004), and Desch (2004) showed that the growth of the MRI is damped when the collision frequency between the neutrals and the ions is smaller than the orbital frequency. This is intuitive; neutrals need to communicate with the ions faster than the timescale over which the MRI acts (i.e., the dynamical one) in order for the neutrals to feel any MRI-like effect at all.

Initial two and three-dimensional simulations of non-linear MRI turbulence in the presence of ambipolar diffusion were carried out by Low et al. (1995) and Brandenburg et al. (1995), respectively. These authors considered the single-fluid, “strong-coupling” limit, valid when the recombination timescale is much shorter than the dynamical time. This limit is generally applicable to protoplanetary disks (Bai & Stone 2011; Bai 2011a). Their results agreed with the expectations of linear theory (Blaes & Balbus 1994); the MRI only operates if

the collision frequency between neutrals and ions exceeds the angular frequency. Simulations in the alternate regime, where the recombination timescale for electrons is assumed to be very long, were conducted by Hawley & Stone (1998) using a two-fluid approach in which the ions and neutrals were evolved separately, only interacting through collisions. The primary result of this work was that for a collision frequency less than 0.01Ω , the ions and neutrals behave independently, but for a frequency larger than 100Ω , the gas behaves as though its fully ionized. When both the collision and orbital frequencies are comparable, the saturation level of the turbulence is primarily controlled by the ion density.

The importance of ambipolar diffusion in the outer regions of protoplanetary disks, the advent of well-resolved mm-wave observations of these regions, and advances in numerical techniques, all motivate more detailed studies of how ambipolar diffusion affects the saturated state of the MRI. Bai & Stone (2011) carried out shearing box simulations in the strong-coupling limit to determine how the MRI saturation level correlates with dimensionless number, Am , defined as the frequency for the neutrals to collide with the ions divided by the orbital frequency (see § 2.1). They found that for simulations with a net toroidal magnetic flux, but no vertical magnetic flux, the turbulence dies away for $\text{Am} \leq 1$, in line with previous studies. For sustained turbulence runs, the saturated turbulent stresses increase with increasing Am , eventually asymptoting towards the ideal MHD level. However, in the presence of a net vertical magnetic flux, turbulence can always be sustained even for $\text{Am} < 1$, assuming that the background vertical magnetic flux is weak enough. For low Am values, however, the resulting turbulence levels are fairly small.

Following these lines of investigation, we study the effect of ambipolar diffusion on the MRI in the outer region of protoplanetary disks by performing numerical simulations using a more realistic disk structure than attempted previously. We include vertical stratification (absent in all prior work except for that of Brandenburg et al. (1995)), which has been shown in some previous MRI calculations to lead to significant qualitative changes in the non-linear evolution. For example, Davis et al. (2010) showed that in the ideal MHD case, the turbulence properties converge with numerical resolution, while in unstratified simulations (and for a vertical domain size of one scale height or less, (Stone, private communication)), the stress level decreases with resolution with no signs of convergence (Fromang & Papaloizou 2007). Similarly, Simon et al. (2011b) showed that in the presence of Ohmic resistivity, vertical gravity can lead to large amplitude fluctuations in the stress levels, a behavior that is absent without vertical gravity.

We also aim to translate our idealized understanding of the ambipolar-dominated MRI into predictions for turbulence and accretion in the outer regions of protoplanetary disks. We run simulations that mimic realistic conditions in the outer disk (which reflect the chemistry calculations in Bai (2011a) and the FUV ionization model of Perez-Becker & Chiang (2011b)). These simulations will provide a quantitative measure of the turbulent saturation, structure, and evolution of the outer disk regions.

Our investigation is divided into two sets of studies, using different magnetic configurations. The first, which we

pursue here (Paper I), assumes zero net vertical magnetic flux⁷. Although it is unlikely that there will be exactly zero vertical magnetic flux penetrating any given region of a disk, this is the most studied field configuration in the literature (e.g., Stone et al. 1996; Fleming & Stone 2003), and it allows us to make direct comparisons between the ambipolar MRI and the previous simulations that include either Ohmic resistivity or assume the gas is fully ionized. It is also possible (though, not particularly likely) that there will be some regions of protoplanetary disks that have negligible vertical magnetic fields; our results will apply to such regions. The second set of studies *will* include a non-zero vertical net magnetic flux, and we defer that problem to Paper II.

The structure of the paper is as follows. In Section 2, we describe our equations, the methods used to solve them and the initial conditions for our simulations. In Section 3.1, we study the effect of Am (here assumed constant in space and time) on vertically stratified MRI turbulence. Then, in Section 3.2, we apply a realistic protoplanetary disk model to allow for a spatially and temporally varying Am. Section 4 discusses the implications of our results for real protoplanetary disks, and we wrap up with conclusions in Section 5.

2. METHOD

2.1. Numerical Method

In this study, we use *Athena*, a second-order accurate Godunov flux-conservative code for solving the equations of MHD. *Athena* uses the dimensionally unsplit corner transport upwind (CTU) method of Colella (1990) coupled with the third-order in space piecewise parabolic method (PPM) of Colella & Woodward (1984) and a constrained transport (CT; Evans & Hawley 1988) algorithm for preserving the $\nabla \cdot \mathbf{B} = 0$ constraint. We use the HLLD Riemann solver to calculate the numerical fluxes (Miyoshi & Kusano 2005; Mignone 2007). A detailed description of the base *Athena* algorithm and the results of various test problems are given in Gardiner & Stone (2005), Gardiner & Stone (2008), and Stone et al. (2008).

Our set up is specialized and necessarily more complex than the base algorithm. First, our simulations utilize the shearing box approximation, which is a model for a local, co-rotating disk patch whose size is small compared to the radial distance from the central object, R_0 . This allows the construction of a local Cartesian frame (x, y, z) that is defined in terms of the disk's cylindrical co-ordinates (R, ϕ, z') via $x = (R - R_0)$, $y = R_0\phi$, and $z = z'$. The local patch co-rotates with an angular velocity Ω corresponding to the orbital frequency at R_0 , the center of the box; see Hawley et al. (1995). Thus, the equations to solve are:

$$\frac{\partial \rho}{\partial t} + \nabla \cdot (\rho \mathbf{v}) = 0, \quad (1)$$

$$\begin{aligned} \frac{\partial \rho \mathbf{v}}{\partial t} + \nabla \cdot (\rho \mathbf{v} \mathbf{v} - B\mathbf{B}) + \nabla \left(P + \frac{1}{2} B^2 \right) \\ = 2q\rho\Omega^2 x - \rho\Omega^2 z - 2\Omega \times \rho \mathbf{v} \end{aligned} \quad (2)$$

⁷ Of course due to the dynamo action of the MRI (Davis et al. 2010; Simon et al. 2011b), the net radial and toroidal fields are allowed to evolve in time.

$$\frac{\partial \mathbf{B}}{\partial t} - \nabla \times (\mathbf{v} \times \mathbf{B}) = \nabla \times \left[\frac{(\mathbf{J} \times \mathbf{B}) \times \mathbf{B}}{\gamma \rho_i \rho} \right], \quad (3)$$

where ρ is the mass density, $\rho \mathbf{v}$ is the momentum density, \mathbf{B} is the magnetic field, P is the gas pressure, and q is the shear parameter, defined as $q = -d\ln\Omega/d\ln R$. We use $q = 3/2$, appropriate for a Keplerian disk. We assume an isothermal equation of state $P = \rho c_s^2$, where c_s is the isothermal sound speed. From left to right, the source terms in equation (2) correspond to radial tidal forces (gravity and centrifugal), vertical gravity, and the Coriolis force. The source term in equation (3) is the effect of ambipolar diffusion on the magnetic field evolution, where ρ_i is the ion density, and γ is the coefficient of momentum transfer for ion-neutral collisions. Note that our system of units has the magnetic permeability $\mu = 1$, and the current density is

$$\mathbf{J} = \nabla \times \mathbf{B}. \quad (4)$$

Adopting this shearing box approximation allows for better resolution of small scales within the disk, at the expense of excluding global effects (those of scale $\sim R_0$). These scales could be physically important (Sorathia et al. 2012; Simon et al. 2012). However, the trade-off is worthwhile for our purposes, because we need to study not only models where ambipolar diffusion is dominant, but also situations where diffusion is *only* important on small scales.

The numerical integration of the shearing box equations require additions to the *Athena* algorithm, the details of which can be found in Stone & Gardiner (2010) and the Appendix of Simon et al. (2011b). Briefly, Crank-Nicholson differencing is used to conserve epicyclic motion exactly and orbital advection to subtract off the background shear flow (Stone & Gardiner 2010). The y boundary conditions are strictly periodic, whereas the x boundaries are shearing periodic (Hawley et al. 1995). The vertical boundaries are the outflow boundary conditions described in Simon et al. (2011b). The electromotive forces (EMFs) at the radial boundaries are properly remapped to guarantee that the net vertical magnetic flux is strictly conserved to machine precision using CT (Stone & Gardiner 2010). In this paper, we only consider the case of zero net vertical magnetic flux; thus, the methods we employ preserve this zero flux condition to machine accuracy.

The integration of the ambipolar diffusion term also requires some modifications to the algorithm. Ambipolar diffusion is implemented in a first-order operator-split manner as in Bai & Stone (2011); the ambipolar diffusion term is integrated separately from the ideal MHD integrator. Furthermore, as is evident from equation (3), the ambipolar diffusion term can be written as an EMF. Thus integrating it is done via the CT method to preserve $\nabla \cdot \mathbf{B} = 0$. The ambipolar diffusion EMFs are also remapped at the radial boundaries in the same way as the ideal MHD EMFs in order to maintain a zero vertical magnetic flux. In addition, before even remapping these ambipolar diffusion EMFs at the radial boundaries, we also remap the toroidal current densities J_y (located at cell edges) so that the line integral $\int J_y dy$ along the inner and outer radial boundaries are equal. We find that this procedure is essential to avoid spurious numerical

features at shearing-box boundaries.⁸

Throughout this paper, the strength of ambipolar diffusion will be characterized by the ambipolar Elsasser number

$$\text{Am} \equiv \frac{\gamma \rho_i}{\Omega}, \quad (5)$$

which corresponds to the number of times a neutral molecule collides with the ions in a dynamical time (Ω^{-1}). Am can be rewritten as

$$\text{Am} = \frac{v_A^2}{\eta_A \Omega}, \quad (6)$$

which is a form reminiscent of the Ohmic Elsasser number. As shown by equation (5), Am is independent of the Alfvén speed; this comes about because the ambipolar diffusivity, η_A is defined as

$$\eta_A \equiv \frac{v_A^2}{\gamma \rho_i}. \quad (7)$$

This diffusivity is responsible for determining the diffusive time step in a Courant limited calculation; $\Delta t_{\text{diff}} \propto \Delta x^2 / \eta_A$. Since the diffusivity is proportional to the Alfvén speed squared, it can become very large in the upper disk regions, making the Courant limited time step extremely small in some of our calculations.

To circumvent this issue, we have implemented the super time-stepping (STS) technique of Alexiades et al. (1996) to accelerate our calculations. The STS technique has already been successfully implemented and tested for studying ambipolar diffusion in multi-fluid codes by O’Sullivan & Downes (2006) and O’Sullivan & Downes (2007) and in a single-fluid code by Choi et al. (2009). Our implementation is similar to theirs, as we describe in detail in the Appendix.

2.2. Am Profiles

For most of our simulations, we fix Am to be constant in order to study the effect of ambipolar diffusion on the non-linear saturation of the MRI in the presence of vertical stratification. This is designed to be the next logical step in extending the work of Bai & Stone (2011) where vertical stratification was not included. We have considered Am=1, 10, 100, 300, 10^3 and 10^4 . Although this prescription of a constant Am profile is highly simplified, it is a necessary, incremental step between the constant Am models without vertical gravity (Bai & Stone 2011) and simulations that incorporate a more realistic prescription for ambipolar diffusion, which we also carry out (see below).

The results of Bai (2011a) show that the physical value of Am in the outer regions of PPDs is of order unity or less. Recently, Perez-Becker & Chiang (2011b) pointed out that the surface layer of protoplanetary disks should be much better ionized due to far ultraviolet (FUV) photon ionization from the central star; these photons almost fully ionize the carbon and sulfur to overcome the effects of recombination onto dust grains. Their results imply

⁸ We note that strict magnetic flux conservation (remap of the EMFs) was not enforced in Bai & Stone (2011), in which case this additional remap of J_y was not necessary. Nevertheless, the variations in vertical net magnetic flux in Bai & Stone (2011) simulations were tiny (less than 0.01%), which did not affect their results.

a large ionization fraction ($f \sim 10^{-5}$) down to a small penetration depth of $\Sigma_{\text{FUV}} \sim 0.01 - 0.1 \text{ g cm}^{-2}$, relatively independent of disk radius. Such an ionization fraction should significantly reduce the strength of ambipolar diffusion (i.e., increase Am) in the disk surface layers.

Thus, in our second set of simulations, we include the effect of FUV ionization at the disk surface layers to give Am a more realistic spatial and temporal dependence. Since we are not including Ohmic resistivity (Gammie 1996) in our calculations, these particular models are only appropriate for the outer regions of protoplanetary disks (e.g., beyond $\sim 10 \text{ AU}$) where ambipolar diffusion dominates Ohmic diffusion (Kunz & Balbus 2004; Armitage 2011). We adopt a minimum-mass solar nebular disk model with surface density of $\Sigma = 1700 R_{\text{AU}}^{-3/2} \text{ g cm}^{-2}$ (Weidenschilling 1977; Hayashi 1981), where R_{AU} is the disk radius measured in AU. We can express the value of Am within the FUV ionized layer as follows (Bai & Stone 2012)

$$\text{Am}_{\text{FUV}} \approx 3.3 \times 10^7 \left(\frac{f}{10^{-5}} \right) \left(\frac{\rho}{\rho_{0,\text{mid}}} \right) R_{\text{AU}}^{-5/4}, \quad (8)$$

where f is the ionization fraction and $\rho_{0,\text{mid}}$ is the mid-plane density. For simplicity, we fix $f = 10^{-5}$, $\rho_{0,\text{mid}} = 1$, and assume a penetration depth of $\Sigma_{\text{FUV}} = 0.1 \text{ g cm}^{-2}$ (which is slightly different from that in Bai & Stone 2012). We conduct two simulations that correspond to radial locations at $R = 30 \text{ AU}$ and $R = 100 \text{ AU}$. Assuming the density profile is Gaussian (see Equation (12)), one finds that the base of the FUV layer (at which the column density equals Σ_{FUV}) is located at $z_b = 1.7H$ for $R = 30 \text{ AU}$ and $z_b = 1.1H$ for $R = 100 \text{ AU}$ (H is the vertical scale height as defined in equation (13) below). In our simulations, we set Am=1 for $-z_b < z < z_b$ as a proxy based on the calculations of Bai (2011a), and use Equation (8) for the ionized surface layers of the disk. In principle, Am < 1 with the inclusion of grains (Bai 2011a). However, as we will see, for Am = 1 ambipolar diffusion is sufficiently strong to quench the MRI in this mid-plane region; thus, going to lower values of Am is unnecessary for the purposes of this study. Finally, we keep the value of z_b fixed throughout the calculation for simplicity.

From these considerations, the value of Am changes quite dramatically from Am=1 to Am $\approx 3 \times 10^4$ at the base of the FUV layer. This very large transition is smoothed over roughly 7 grid zones so as to prevent a discontinuous transition in Am. The smoothing functions we apply are based upon the error function (ERF). Thus, the complete profile of Am for these runs is given by

$$\text{Am} \equiv \begin{cases} \text{Am}_{\text{FUV}} & z \geq z_b + \Delta z \\ 1 + \frac{1}{2} \text{Am}_{\text{FUV}} S^+(z) & z_b - n\Delta z < z < z_b + \Delta z \\ 1 & -z_b + n\Delta z \leq z \leq z_b - n\Delta z \\ 1 + \frac{1}{2} \text{Am}_{\text{FUV}} S^-(z) & -z_b - \Delta z < z < -z_b + n\Delta z \\ \text{Am}_{\text{FUV}} & z \leq -z_b - \Delta z \end{cases} \quad (9)$$

where $S^+(z)$ and $S^-(z)$ are the smoothing functions defined as

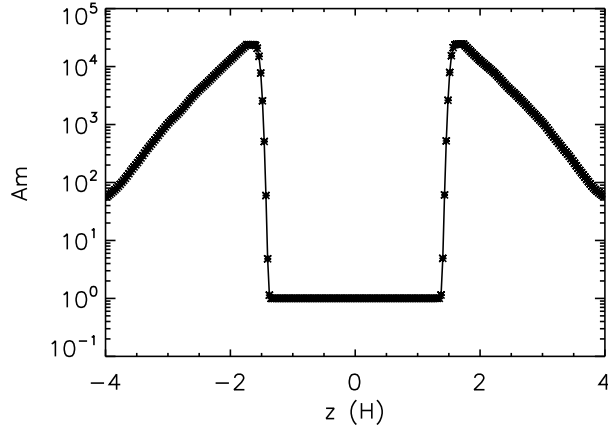


FIG. 1.— Vertical profile for Am at $R_{AU} = 30$. The profile corresponds to the initial time of Z30AU, which is orbit 22 from the $Am = 10^5$ run with the same domain size. The value of Am has been averaged horizontally. The units of the x axis are the vertical scale height, H . The asterisks denote the locations of grid zones. Am transitions from $Am = 1$ to $Am = Am_{FUV}$ (as defined in the text), and this transition is smoothed over roughly 7 grid zones using the error function.

$$S^+(z) \equiv 1 + \text{ERF}\left(\frac{z - 0.9z_b}{\Delta z}\right), \quad (10)$$

$$S^-(z) \equiv 1 - \text{ERF}\left(\frac{z + 0.9z_b}{\Delta z}\right), \quad (11)$$

Here, $n = 8$ and $\Delta z = 0.05H$. These numbers were chosen to give a reasonably resolved transition region between $Am = 1$ and Am_{FUV} . For a visual representation of the rather complex equation (9), we plot in Fig. 1 the vertical profile of Am (averaged over x and y) for the run at $R_{AU} = 30$ at the initial time, referring here to when the run was restarted from C1e5 (see below). The asterisks denote the grid cell centers; as previously mentioned, the transition region is resolved by ~ 7 zones.

2.3. Simulations

We have run simulations with several domain sizes and Am profiles. All of the simulations with $Am < 10^5$ or with spatially and temporally varying Am are initialized from the turbulent state of a “starter” calculation with the same domain size but with $Am = 10^5$ (i.e., reasonably close to ideal MHD).

These starter simulations are initialized with a density corresponding to isothermal hydrostatic equilibrium.

$$\rho(x, y, z) = \rho_0 \exp\left(-\frac{z^2}{H^2}\right), \quad (12)$$

where $\rho_0 = 1$ is the mid-plane density, and H is the scale height in the disk,

$$H = \frac{\sqrt{2}c_s}{\Omega}. \quad (13)$$

The isothermal sound speed, $c_s = 7.07 \times 10^{-4}$, corresponding to an initial value for the mid-plane gas pressure of $P_0 = 5 \times 10^{-7}$. With $\Omega = 0.001$, the value for the scale height is $H = 1$. A density floor of 10^{-4} is

applied to the physical domain as too small a density leads to a large Alfvén speed and a very small time step. Furthermore, numerical errors make it difficult to evolve regions of very small plasma β (ratio of thermal pressure to magnetic pressure).

The initial magnetic field is purely toroidal and has a constant $\beta = 100$ throughout the domain (thus, B_y^2 has a Gaussian shape like the density). Random perturbations are added to the density and velocity components to seed the MRI.

The remaining simulations are restarted from orbit 50 (orbit 22 for the simulations with domain size $8H \times 16H \times 8H^9$) of their corresponding domain size simulation with $Am = 10^5$. They are listed in Table 1. The label for each calculation describes whether the value of Am is constant with height, labeled C, or varies according to equation (9), labeled Z. For the constant Am simulations, the number following the C is the value of Am . For the spatially varying Am calculations, the number afterwards (along with the AU) describes the radial location of the shearing box in our protoplanetary disk model in units of AU. An S (L) following the Am value corresponds to a domain size of $2H \times 4H \times 8H$ ($8H \times 16H \times 8H$), which is smaller (larger) than the $4H \times 8H \times 8H$ size of most of the constant Am calculations. The “starter” simulation for the $4H \times 8H \times 8H$ runs is also included in the table, labeled C1e5. Finally, all of our calculations are carried out at a resolution of 36 grid zones per H .

3. RESULTS

3.1. Constant Am Calculations

We begin by applying some standard diagnostics to the set of calculations with constant values of Am . The first such diagnostic is the density-weighted Maxwell and Reynolds stresses (see equation (37) of Balbus & Hawley 1998), defined as

$$W_{R\phi} = \frac{\langle \rho v_x \delta v_y - B_x B_y \rangle}{\langle \rho \rangle} \quad (14)$$

where the angled brackets denote a volume average over the whole domain. Figure 2 shows the time evolution of this total stress for the $4H \times 8H \times 8H$ runs, normalized by the square of the sound speed. The dashed line indicates the averaged value (from orbit 25 to 53) of the run with $Am = 10^5$ from which all of the other $4H \times 8H \times 8H$ runs were restarted. The different Am values are denoted by the color. The runs with $Am > 1$ appear to adjust on a roughly 50 orbit timescale after which a statistical steady state follows. In general, the stress increases with increasing Am (decreasing diffusion) for these runs. However, the $Am = 10$ and $Am = 100$ runs have roughly the same values at late times, as do the $Am = 300$, 1000, and 10000 runs.

The $Am = 1$ case deserves extra attention. From Fig. 2, it would appear that the turbulence completely

⁹ We choose a different restart time for these calculations because we decided midway through running our simulations that a larger number of cores is significantly more efficient for the variable Am runs. Thus, we had to redo the $Am = 10^5$ calculations, and orbit 22 was chosen because the density-weighted stress at this time was roughly equal to orbit 50 of the lower core version of this calculation.

TABLE 1
SHEARING BOX SIMULATIONS

Label	Ambipolar Diffusion	Domain Size ($L_x \times L_y \times L_z$) H	α
C1	Am = 1, constant	$4 \times 8 \times 8$	decayed
C10	Am = 10, constant	$4 \times 8 \times 8$	0.0046
C10L	Am = 10, constant	$8 \times 16 \times 8$	0.0055
C100S	Am = 100, constant	$2 \times 4 \times 8$	0.070
C100	Am = 100, constant	$4 \times 8 \times 8$	0.0062
C300	Am = 300, constant	$4 \times 8 \times 8$	0.024
C1000	Am = 1000, constant	$4 \times 8 \times 8$	0.022
C10000	Am = 10^4 , constant	$4 \times 8 \times 8$	0.025
C1e5	Am = 10^5 , constant	$4 \times 8 \times 8$	0.038
Z30AU	Am at $R = 30$ AU	$8 \times 16 \times 8$	0.0016
Z100AU	Am at $R = 100$ AU	$8 \times 16 \times 8$	0.0015

dies away. A closer examination of the stress histories show that the Maxwell stress levels out to a small, but positive value, while continuing to slowly decrease with time. The Reynolds stress approaches an oscillatory behavior which occasionally brings it below zero. Space-time plots of various quantities in this run indicate that the gas is no longer MRI turbulent. The remnant Maxwell stress is the result of a residual large scale B_x and B_y field near the mid-plane, and the Reynolds stress appears to arise from residual waves propagating through the box. The longer term behavior of this Am value could not be examined because even with STS, the diffusion limited time step is very small for Am = 1; running it out further would be very computationally expensive. However, these results strongly indicate that the MRI turbulence has completely decayed away, consistent with the results of Bai & Stone (2011). This behavior will play an important role in the variable Am simulations of Section 3.2.

We time-average this normalized stress and define the Shakura-Sunyaev α parameter,

$$\alpha = \frac{\overline{W_{R\phi}}}{c_s^2} \quad (15)$$

where the overbar denotes the time average, which is done from orbit 100 onwards for most of the constant Am runs with Am > 1; from orbit 72 onwards for runs C10L, Z30AU, and Z100AU; and from orbit 25 to 53 for the Am = 10^5 “starter” simulation. Fig. 3 displays α versus Am for these runs. The arrow on the Am = 1 run indicates that the stress level is continually decreasing. The trend of α with Am can be compared with the unstratified simulations shown in Fig. 10 of Bai & Stone (2011). These trends roughly agree, though the results from Bai & Stone (2011) show a monotonic increase of α with Am, whereas our results show that different Am values can lead to very similar α values.

This difference may be attributable to different background magnetic field strengths as the background field evolves via the usual MRI dynamo (e.g., Davis et al. 2010; Simon et al. 2011b). To understand this further, first let us consider the space time diagrams of the toroidal field B_y for C10, C100, C300, and C1000 as shown in Fig. 4. In these diagrams, the field has been averaged over x and y and is plotted in the (t, z) plane. The most obvious feature from these diagrams is that the period of the dynamo flipping of B_y changes with

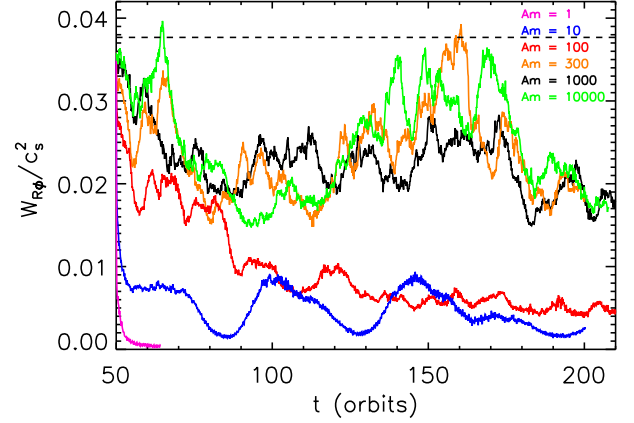


FIG. 2.— Density-weighted volume average of the total (Maxwell and Reynolds) stress, normalized by the square of the sound speed, versus time for the standard $4H \times 8H \times 8H$ simulations. The magenta line corresponds to Am = 1, blue to Am = 10, red to Am = 100, orange to Am = 300, black to Am = 1000, and green to Am = 10^4 . The horizontal dashed line corresponds to the time-averaged (from orbit 25 to 53) stress value for Am = 10^5 from which the other runs were initialized. After an initial transient of ~ 50 orbits, the simulations with Am $\gtrsim 10$ are sustained. There is a general trend of increasing stress level with increasing Am. The Am = 1 case has turbulence that decays away rapidly.

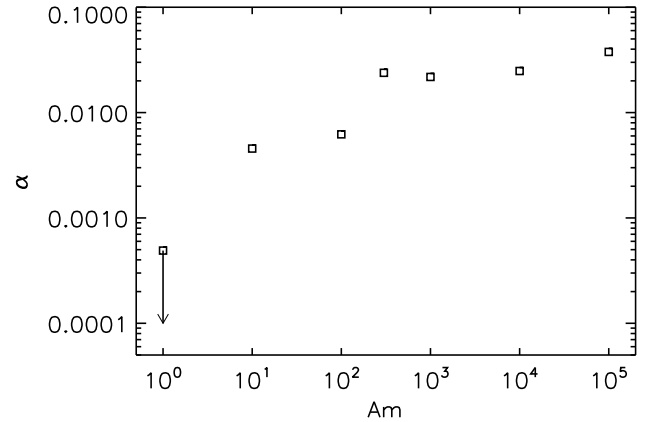


FIG. 3.— Time-averaged total stress (i.e., α) as a function of Am for the standard $4H \times 8H \times 8H$ simulations. There is a general trend of increasing stress level with increasing Am.

Am; as ambipolar diffusion becomes stronger, the period increases. In particular, for Am = 10, the period is ~ 50 orbits, and for Am = 100 (only considering times past the initial 50 orbit transient period), the period is $\sim 15 - 20$ orbits. For Am ≥ 300 , the period is ~ 10 orbits as is usually observed in stratified MRI simulations.

The most relevant feature here, however is that the background toroidal field strength is different for different values of Am. In Bai & Stone (2011), it was found that with zero net vertical flux, the stress level increases with increasing net toroidal flux (which is mostly conserved in unstratified simulations). Therefore, in our stratified simulations, *two* effects are expected to determine the saturated stress values: the value of Am and the

background toroidal field strength, set by the dynamo. To demonstrate this effect more robustly, we calculate a version of the plasma β for the background toroidal field,

$$\beta_y \equiv 2\overline{\langle P \rangle} / \overline{\langle B_y \rangle^2}, \quad (16)$$

where the overbars indicate a time average (from orbit 100 onwards) and the angled brackets denote an average over x and y . This quantity is representative of the amplitude of the oscillating background toroidal field. β_y is a function of z only, and we plot it along with the vertical profile of the total stress (which has again, been averaged in time and for all x and y) in Fig. 5.

The stress profile reveals the same behavior as that in Fig. 3; there is a general trend of increasing stress with increasing Am . Furthermore, this increase occurs uniformly across all z . However, C300 and C1000 have roughly the same stress profiles, and C10 peaks at around the same value as C100. Examining the β_y for these particular simulations, we see that C300 has a lower value (stronger field) than does C1000. Similarly, C10 has a significantly smaller β_y than C100. These results confirm that it is indeed the larger background toroidal field strength that make the stress levels in run C10 approach that in run C100, and the stress in run C300 approach that in run C1000. We note, however, that C1000 and C10000 have both the same β_y profiles and the same stress profiles. This could indicate that for $Am > 1000$, the turbulence levels are approaching that of ideal MHD. The slightly higher stress for C1e5 would then be explained by its lower β_y .

It remains unclear why the background field strength varies in the way that it does. Could this also be controlled by the value of Am ? This is not unreasonable considering that ambipolar diffusion already affects the period of the toroidal field flipping. The question of exactly how Am and the dynamo are related is very open. Unfortunately, exploring it in detail would take us too far from our goals in this paper, and so, we leave it for future work.

The final diagnostic we employ is the two-point autocorrelation function first used in the context of MRI simulations in Guan et al. (2009). We employ this diagnostic for similar reasons as those in Simon et al. (2012); we wish to determine the structure of the turbulent magnetic field and check that the domain sizes we use are sufficiently large to properly capture important turbulent scales. Thus, we define the autocorrelation function of the i^{th} component of the *perturbed* magnetic field as

$$\text{ACF}(\delta B_i(\Delta \mathbf{x})) = \frac{\int \delta B_i(t, \mathbf{x}) \delta B_i(t, \mathbf{x} + \Delta \mathbf{x}) d^3 \mathbf{x}}{\int \delta B_i(t, \mathbf{x})^2 d^3 \mathbf{x}}, \quad (17)$$

where δB_i is the value of B_i after subtracting off the horizontal mean field. In equation form,

$$\delta B_i(x, y, z) \equiv B_i(x, y, z) - \langle B_i \rangle_{xy}(z), \quad (18)$$

and the average denoted by $\langle \rangle_{xy}$ is the horizontal average. We have defined the ACF to be normalized by its maximum value (at $\Delta x = \Delta y = \Delta z = 0$). The ACF of the total turbulent magnetic field is then defined as $\text{ACF}(\delta B) = \text{ACF}(\delta B_x) + \text{ACF}(\delta B_y) + \text{ACF}(\delta B_z)$. The overbar denotes a time average done from orbit 100 to

125 in all cases.

From the figure, it appears that the $Am = 100$ ACF is roughly consistent between a domain size of $2H \times 4H \times 8H$ and $4H \times 8H \times 8H$, though there is a slight difference in the size of the tilted centroid. However, as we will see shortly, $2H \times 4H \times 8H$ is actually too small for $Am = 100$. The standard box size, $4H \times 8H \times 8H$, appears to properly contain the ACF for $Am = 100$, but not as well for $Am = 10$. The centroid of the $Am = 10$ case is larger and appears to have a longer tail that intersects the toroidal boundary. Going to an even larger domain, $8H \times 16H \times 8H$, the $\text{ACF}(B)$ for $Am = 10$ looks more well contained, though the very end of the tail does appear to touch the toroidal boundary. This effect is not as dramatic as in the smaller domain. Going to an even larger domain and running $Am = 10$ is prohibitively expensive given our current computational resources.

Returning to the smallest domain, we note some odd features. Despite the reasonable ACF, an inspection of the stress history and the α value (see Table 1) show this calculation to be quite different than $Am = 100$ at larger domain sizes. An examination of the space-time evolution of B_y , Fig. 7, brings the point home further, as it indicates that the dynamo behavior is completely shut off for this particular run. This is again inconsistent with the larger domain $Am = 100$. Thus, we conclude that $2H \times 4H \times 8H$ is too small of a domain for $Am = 100$ and will likely be too small for smaller values of Am as well.

As indicated by these results, the standard box size of $4H \times 8H \times 8H$ is large enough for all of our simulations except for $Am \leq 10$. It is computationally too expensive for us to run all of our simulations at the larger $8H \times 16H \times 8H$. So, we elect to use the smaller size as our standard, and we compare the evolution of the stress between the $4H \times 8H \times 8H$ and $8H \times 16H \times 8H$ domains for $Am = 10$ to justify using a smaller domain for comparison between $Am = 10$ and other Am values. Figure 8 shows the $W_{R\phi}$ evolution for these two domain sizes with $Am = 10$. The use of a smaller domain size does not appear to make a difference for this value of Am . Furthermore, the B_y space-time plot for the larger domain looks very similar to the smaller domain. Evidently, we can get away with using a smaller domain for $Am = 10$. However, these ACFs suggest that caution be used when running ambipolar diffusion shearing box calculations.

One final thing to note from $\text{ACF}(B)$ is that as Am is decreased, the tilted centroid component appears to become more elongated (hence the need for larger domains) and less tilted with respect to the y axis.

To summarize this section, we find the turbulent stress level dependence on Am in vertically stratified simulations to be generally consistent with the results of unstratified simulations (Bai & Stone 2011); α increases with Am , and for $Am \lesssim 1$, there is no turbulence. We also find that as Am is decreased, larger domain sizes are needed in order to properly capture the turbulent structures represented by the ACF. These runs serve as a baseline for interpreting the results from the next section, in which Am varies spatially and temporally based upon our model for surface layer ionization.

3.2. Variable Am Calculations

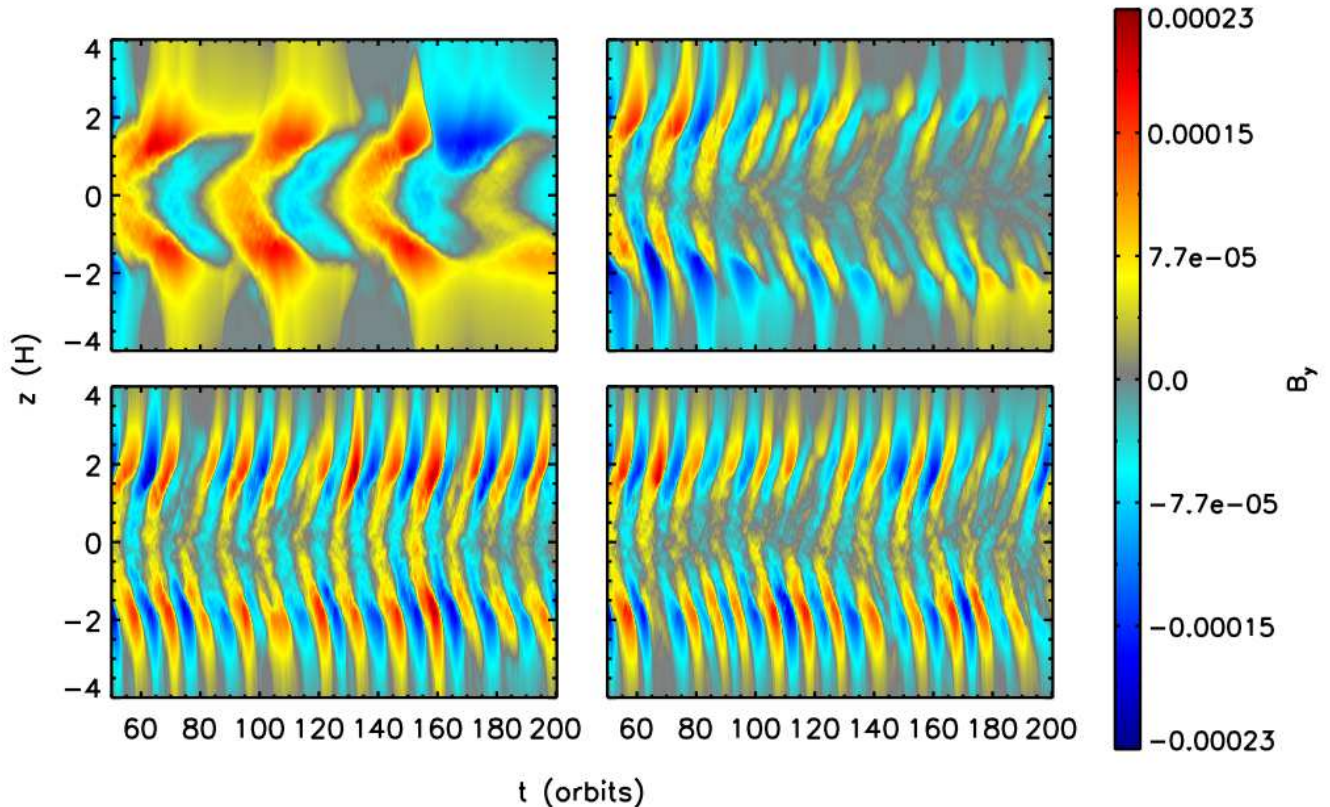


FIG. 4.— Space-time plot of B_y averaged over x and y for $Am = 10$ (upper left), $Am = 100$ (upper right), $Am = 300$ (lower left), and $Am = 1000$ (lower right). The “butterfly” dynamo is present in all simulations, but the period of the B_y flipping increases with decreasing Am . In particular, the period is $\sim 40 - 50$ orbits for $Am = 10$ and $\sim 15 - 20$ orbits for $Am = 100$. For the other two cases, the period is ~ 10 orbits, equal to that in ideal MHD calculations.

We now turn our attention to the two calculations with spatially and temporally varying Am (the “Z” simulations in Table 1). As stated previously, these simulations adopt more realistic non-constant Am values and directly address the questions such as “how vigorous is outer disk MRI-driven turbulence?” or “what is the mass accretion rate in the outer disk?” under the assumption that the outer disk is not threaded by any net vertical magnetic field. We run them all at the largest domain size, $8H \times 16H \times 8H$, because there are regions of $Am \leq 1$ in these calculations.

As before, we begin by examining the density-weighted stress normalized by the square of the sound speed, as shown in Fig. 9. It is clear from the figure that the stress levels are lowered dramatically compared to the ideal MHD case. Indeed, by calculating the average of the curve from orbit 72 onward, we find that the α values are $\sim 10^{-3}$, one order of magnitude below what is expected from observations (Hartmann et al. 1998).

While the turbulence initially decreases drastically, it has not completely died away. Consider the space-time diagrams in the (t, z) plane for various horizontally averaged quantities of run Z100AU, as shown in Fig. 10. From both the Maxwell and Reynolds stress plots, there is a significant region in z over which the MRI is indeed active. The vertical structure is consistent with what we would expect from our ionization profile; there is a sig-

nificant “ambipolar dead zone” corresponding to where $Am = 1$ and the higher Am regions correspond to turbulent activity. We will calculate an actual mass accretion rate at both 30 AU and 100 AU in Section 4.1.

Despite there being very little Maxwell stress in the ambipolar dead zone, there is still Reynolds stress in this region. This stress is likely produced by the active layers, similar to what is observed in simulations that include an Ohmic dead zone (Fleming & Stone 2003). It is possible, however, that as in run C1, the Reynolds stress here is simply left over from the turbulent state from which the run was restarted. To test this notion, we restarted Z100AU at orbit 85 and set all perturbed velocity components to zero throughout the domain (the shear profile is of course maintained). We find that the active MRI layers do indeed induce velocity fluctuations within the ambipolar dead zone, which leads to a positive Reynolds stress on average.

Finally, the horizontally averaged B_y space-time plot shows interesting behavior. Within the ambipolar dead zone, the toroidal field remains fixed in sign, though the magnitude appears to be decreasing. Between 1 and 2 scale heights above and below the mid-plane, the usual MRI dynamo reappears, with a B_y oscillation period of ~ 10 orbits, identical to ideal MHD. Again, from the Maxwell stress plot, it is obvious that this region is turbulent. For $|z| > 2H$, however, there is a strong toroidal

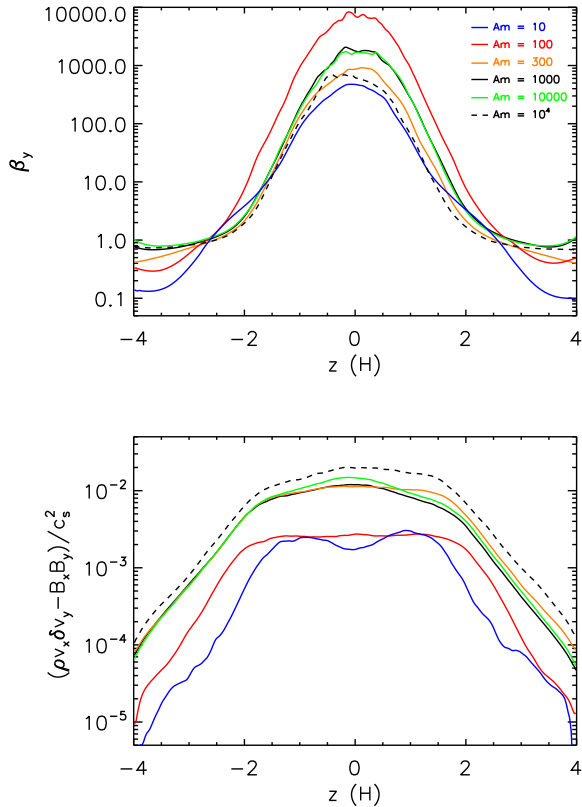


FIG. 5.— Vertical profiles of β_y as defined by equation (16) (top) and the total stress normalized by the square of the sound speed (bottom). The quantities have been averaged over x and y and over time from orbit 100 onwards as described in the text. The blue line corresponds to $Am = 10$, red to $Am = 100$, orange to $Am = 300$, black to $Am = 1000$, green to $Am = 10^4$, and dashed line to $Am = 10^5$ (the time average for this run is done from orbit 25 to the end of the calculation). The stress increases with Am roughly uniformly at all heights. There is no obvious trend between β_y and Am .

field that remains stationary. There are slight changes in magnitude as the toroidal field from the turbulent region propagates outwards.

Examining the same diagrams for Z30AU reveals very similar behavior. There is a thin layer of strong Maxwell and Reynolds stress located around $|z| \sim 2H$, along with a positive Reynolds stress induced in the ambipolar dead zone by the active layers. In this calculation, however, the active region is much narrower in z when compared to Z100AU. This is because the FUV photons do not ionize the disk quite as deep as at $R = 100$ AU, and as is usual, the MRI appears to be inactive for $|z| \gtrsim 2H$. Thus, the MRI-active region is forced to be contained within a smaller z region.

In Simon et al. (2011b), the authors found that the toroidal and radial field in a resistivity dominated mid-plane region evolved in time. Occasionally, the toroidal field grew to strong enough levels that the MRI became temporarily reactivated, after which the Ohmic resistivity quenched the turbulence again. This variability occurred on very long timescales of ~ 100 orbits. In these simulations, we do see that the toroidal field in the ambipolar dead zone changes in amplitude over time. Is it possible, then, that the field could grow to large enough

values to eventually re-activate the MRI in that region? Integrating our simulations out for many hundreds of orbits is prohibitively expensive, and therefore, we will not be able to observe any such variability in our stratified simulations. Instead, we have run an *unstratified* shearing box of size $8H \times 16H \times H$ with $Am = 1$ and uniform toroidal field of strength $\beta = 10$, chosen to determine if a strong toroidal field MRI will be active with $Am = 1$. We start the simulation with a relatively large amplitude perturbation to the density and velocities, such that the initial perturbations should already be reasonably non-linear. As a control, we also ran this identical setup with $Am = 10^5$. With $Am = 1$, we observed decay of the initial perturbations and no development of any MRI turbulence, whereas with $Am = 10^5$, the MRI becomes active and generates sustained turbulence for many orbits. Thus, even in the presence of a strong field, $Am = 1$ is sufficient to quench MRI-driven turbulence. We therefore do not expect the behavior observed in Simon et al. (2011b) to occur in these simulations.

The vertical structure is also depicted via time- and horizontally-averaged quantities as a function of z , as is shown in Fig. 11. From the top two panels, it is obvious that there is a double-peak structure to the stress; no doubt a result of the ambipolar dead zone. Within this dead zone, the Reynolds stress dominates over the Maxwell stress. From the space-time diagrams above, any nonzero Maxwell stress within this region likely results from large scale correlations in the magnetic field rather than any sort of turbulence. Note that there are regions where the stress can go negative, and since the vertical axis is logarithmic, the curves are simply cut off where the values drop below zero.

The bottom two panels show the various energies (i.e., thermal, kinetic, and magnetic) as a function of height. The thermal pressure dominates over the vast majority of the disk's vertical structure. However, for $|z| \gtrsim 2.5H$, the magnetic energy dominates over all other energies. We note in particular the very strong magnetic dominance in the upper z regions of Z30AU (lower left panel). This magnetic field is stationary in time according to the space-time diagram for this run, akin to the lower panel of Fig. 10.

We attribute some of this behavior to the gas density floor. Indeed, looking at the vertical pressure profile (which follows the gas density), the pressure is prevented from going below 10^{-4} of its initial peak value. The resulting gradient in the gas pressure has an effect on the buoyant properties of the field. We address this issue further in the next section.

3.3. The Effect of the Density Floor

To test the effect of lowering the density floor, we restarted simulations C10 and Z30AU at orbits 120 and 56 respectively and lowered the density floor to 3×10^{-5} , roughly 3 times smaller than the original density floor. While this new value for the floor may still be higher than what the density would naturally be, it becomes extremely expensive to run lower density floor calculations even for a short integration. Thus, our main goal in running these calculations is to observe the immediate effect of lowering the floor on properties such as the density-weighted stress and the buoyancy of the magnetic field in the upper disk regions. Is the evolution of the system

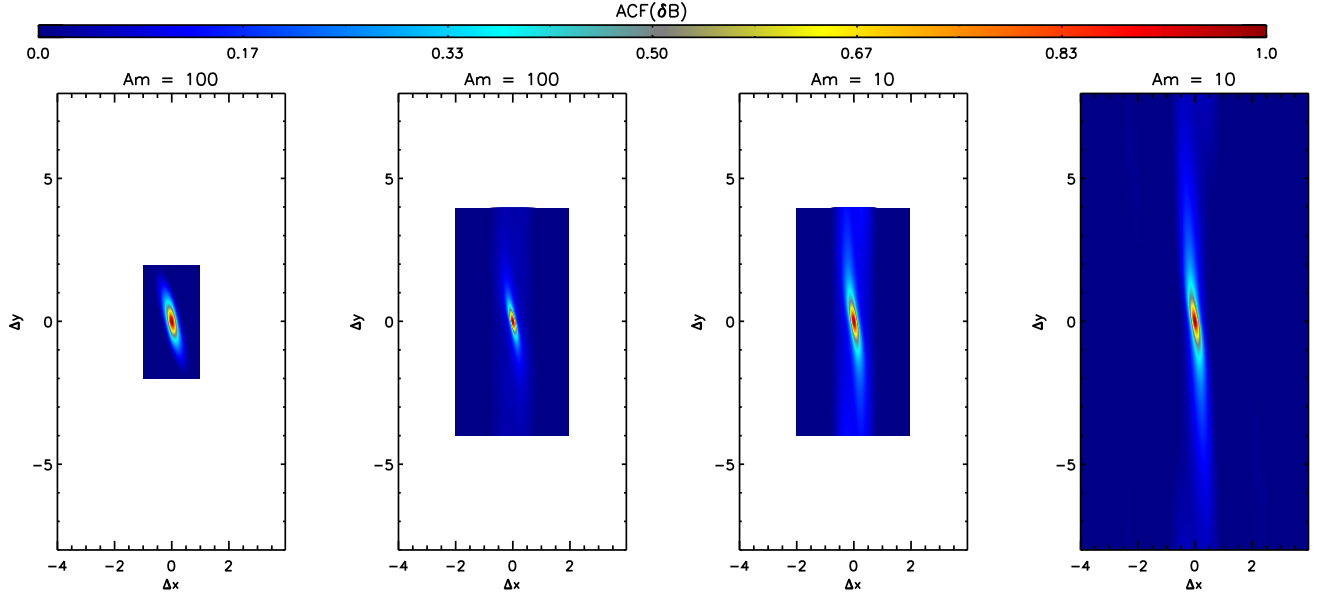


FIG. 6.— Autocorrelation function (ACF) of the magnetic field, as defined by equation (17), for simulations (from left to right) with $Am = 100$ and size $2H \times 4H \times 8H$, $Am = 100$ and size $4H \times 8H \times 8H$, $Am = 10$ and size $4H \times 8H \times 8H$, and $Am = 10$ and size $8H \times 16H \times 8H$. As Am is decreased, larger and larger domains are needed to properly contain the ACF. Furthermore, the tilted centroid feature becomes less tilted with respect to the y axis and more elongated as Am is decreased.

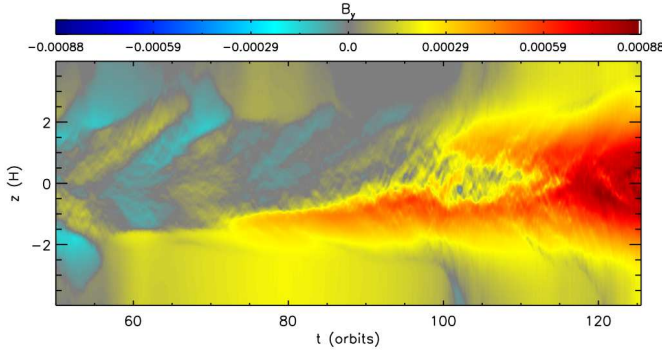


FIG. 7.— Space-time plot of B_y averaged over x and y for the $Am = 100$ run at domain size $2H \times 4H \times 8H$. There is a remnant dynamo behavior that rapidly dies away as the simulation adjusts to the new value of Am . Eventually, the dynamo activity ceases altogether, which is inconsistent with the larger domain counterpart of $Am = 100$. This domain size appears to be too small to properly capture the dynamo at $Am = 100$.

altered drastically? What, if any, changes occur?

Examining the space-time diagrams for these restarted runs indicate that the lowered density floors lead to enhanced buoyancy of the magnetic fields. For example, consider the lower left panel of Fig. 11. Once the floor is lowered, the magnetic energy for $z \lesssim -2H$ immediately drops to lower values as field rises away from the mid-plane.¹⁰ The same behavior is observed in run C10 for both $z \lesssim -2H$ and $z \gtrsim 2H$. Thus, the presence of a strong magnetic field for $|z| > 2H$, as is shown in the lower panel of Fig. 10, is artificial. That being said, based upon the results of ideal MHD calculations (Simon et al.

¹⁰ The field for $z \gtrsim 2H$ does not appear to change significantly over the time that we integrated this simulation. However, we did not evolve this simulation for very long, and we speculate that a longer evolution would show a change in the magnetic field strength in this region.

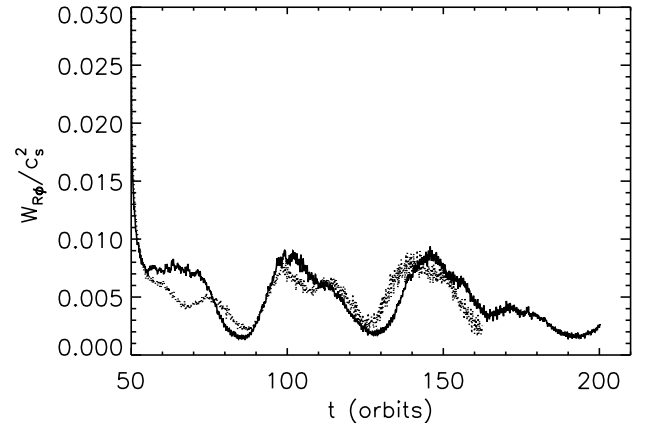


FIG. 8.— Density-weighted volume average of the total (Maxwell and Reynolds) stress, normalized by the square of the sound speed, versus time for the $Am = 10$ simulation at a domain size of $4H \times 8H \times 8H$ (solid line) and $8H \times 16H \times 8H$ (dotted line). Note that the $8H \times 16H \times 8H$ run was restarted from orbit 22 of a different “starter” simulation. For comparison purposes, we translated the solution to the right by 28 orbits. The curves show a nearly identical evolution.

2011b) in which the density is on average larger than the floor value at all locations, we still expect the field to be superthermal in this region; it will just be weaker.

Does this feature affect our main results so far? An examination of the stress evolution shows that the decrease in the density floor does lead to a decrease in the volume-averaged stresses. Quantitatively speaking, in Z30AU, the magnetic energy averaged over $z \leq -2H$ drops by a factor of ~ 4 in going from orbit 56 to 78.5. During this same time, the volume-averaged stresses decrease by a factor of ~ 1.5 , and the stress does not appear to be lev-

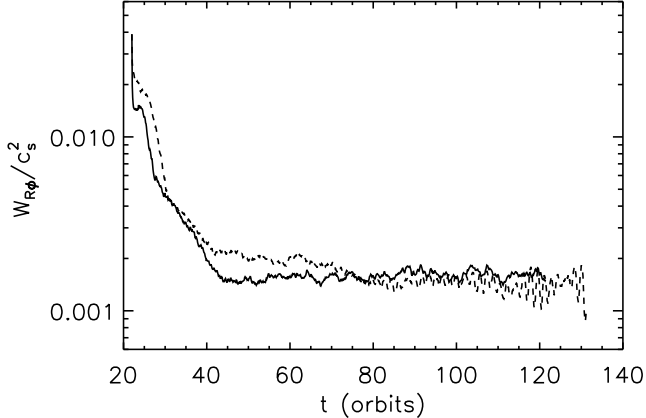


FIG. 9.— Density-weighted volume average of the total (Maxwell and Reynolds) stress, normalized by the square of the sound speed, versus time for the Z30AU simulation (solid line) and the Z100AU simulation (dashed line). The curves show a clear drop from the initial state of vigorous turbulence to levels near $W_{R\phi}/c_s^2 \sim 10^{-3}$.

eling off. Running the simulation out further is computationally prohibitive given the small time step incurred by the lower density floor. So, there *is* an effect due to the density floor. Since we have not fully quantified this effect, it should be borne in mind when we calculate mass accretion rates in Section 4.1. We address the density floor issue again in Section 4.2.

4. IMPLICATIONS FOR PROTOPLANETARY DISK STRUCTURE AND EVOLUTION

4.1. Mass Accretion Rate

One of the most important properties of disk evolution is the mass accretion rate due to angular momentum transport. We can calculate this quantity, \dot{M} , for Z30AU and Z100AU by utilizing equation (40) in Balbus & Hawley (1998), which assumes accretion is in steady-state. We take this equation in the limit that $R \gg R_o$, as appropriate for the shearing box approximation:

$$\dot{M} = \frac{2\pi\Sigma}{\Omega} \overline{W_{R\phi}} \approx 8.5 \times 10^{-6} \alpha R_{AU}^{-1/2} M_{\odot}/\text{yr}, \quad (19)$$

where the expression on the right comes from applying this formula to the minimum mass solar nebula model, and α is defined as in equation (15). The definition of $W_{R\phi}$ in Balbus & Hawley (1998) is the same as ours in the sense that it is a *density weighted* stress. From this equation, we calculate that $\dot{M} \approx 2.5 \times 10^{-9} M_{\odot}/\text{yr}$ at 30 AU and $\dot{M} \approx 1.2 \times 10^{-9} M_{\odot}/\text{yr}$ at 100 AU. Of course, due to the effect from the high density floor (see discussion in Section 3.3), the actual accretion rates are likely to be lower, and these values serve as an upper limit.

These accretion rates are at least one order of magnitude too small (likely even smaller, again due to the density floor) to account for the observed accretion rates in Classical T-Tauri systems (e.g., Hartmann et al. 1998).

We can also compare our results to semi-analytical predictions made by Bai (2011a) based upon the results of unstratified simulations with a net vertical magnetic flux (Bai & Stone 2011). This comparison will allow us to

gauge the potential importance of having a net vertical flux in regions of strong ambipolar diffusion. By first extracting the vertical profiles of ρ and Am , and then by assuming constant magnetic field strength across the MRI active region of the disk, we can estimate the accretion rate for any given field strength using equation (28) of Bai (2011a). From this approach, $\dot{M} = 9.8 \times 10^{-9} M_{\odot}/\text{yr}$ and $3.5 \times 10^{-8} M_{\odot}/\text{yr}$ at 30 AU and 100 AU, respectively, roughly one order of magnitude larger than our calculated rates and in general agreement with observations.

These estimates suggest that it is very likely that a net vertical field is required to attain the necessary turbulence levels, if the MRI is indeed the dominant mechanism by which angular momentum is transported. We will carry out actual shearing box simulations with vertical stratification and ambipolar diffusion in the presence of a net vertical magnetic field in Paper II.

4.2. Turbulent Linewidth

Another property of disks of recent interest has been the density-weighted distribution of turbulent velocities as a function of disk radius and height above the mid-plane. This was first calculated by Simon et al. (2011a) for local MRI simulations without ambipolar diffusion, but including the effects of Ohmic resistivity. Another study, Forgan et al. (2012), carried out a similar analysis for global calculations of self-gravity driven turbulence. These distributions are a first order approach to making a connection with observational constraints of turbulent line broadening in the sub-mm, such as those in Hughes et al. (2011). In particular, the density-weighted velocity distribution represents the probability of observing a line with a particular turbulent velocity broadening.

Here, we carry out an identical analysis to that done in Simon et al. (2011a) for both of our variable Am calculations (see that paper for the exact details of how to calculate the velocity distribution). Figure 12 shows this velocity distribution for Z30AU (top and middle) and Z100AU (bottom). As was observed in Simon et al. (2011a) for their calculations with a strong Ohmic dead zone (see their Fig. 4, top panel), we also observe a strong gradient in peak velocity as one probes deeper towards the mid-plane. Indeed, the mid-plane velocity distribution peaks around $v/c_s \sim 0.01$, just as in the Ohmic case. Furthermore, as one probes the surface layers of the disk $|z| > 3H$, the peak of the distribution occurs around $v/c_s \sim 0.2 - 0.4$. There is also a non-negligible supersonic tail; in Z100AU, this component comprises $\sim 1\%$ of the horizontal and vertical distributions at $z > 3H$. In Z30AU, this component comprises $\sim 2\%$ of the vertical distribution and $\sim 7\%$ of the horizontal distribution at $z < -3H$.

In the top panel of the figure, the red and black curves nearly lie on top of each other. This is likely an artificial effect resulting from the very dominant magnetic field that is stationary for $z > 2H$ in Z30AU (which itself results from the relatively large density floor applied in this calculation). The magnetic field is not nearly as dominant for $z < -2H$ (the other side of the mid-plane), and so the middle panel of Fig. 12 shows the velocity distribution calculated from this side. This distribution looks much more similar to the other distributions.

To further test the effect of the density floor on our

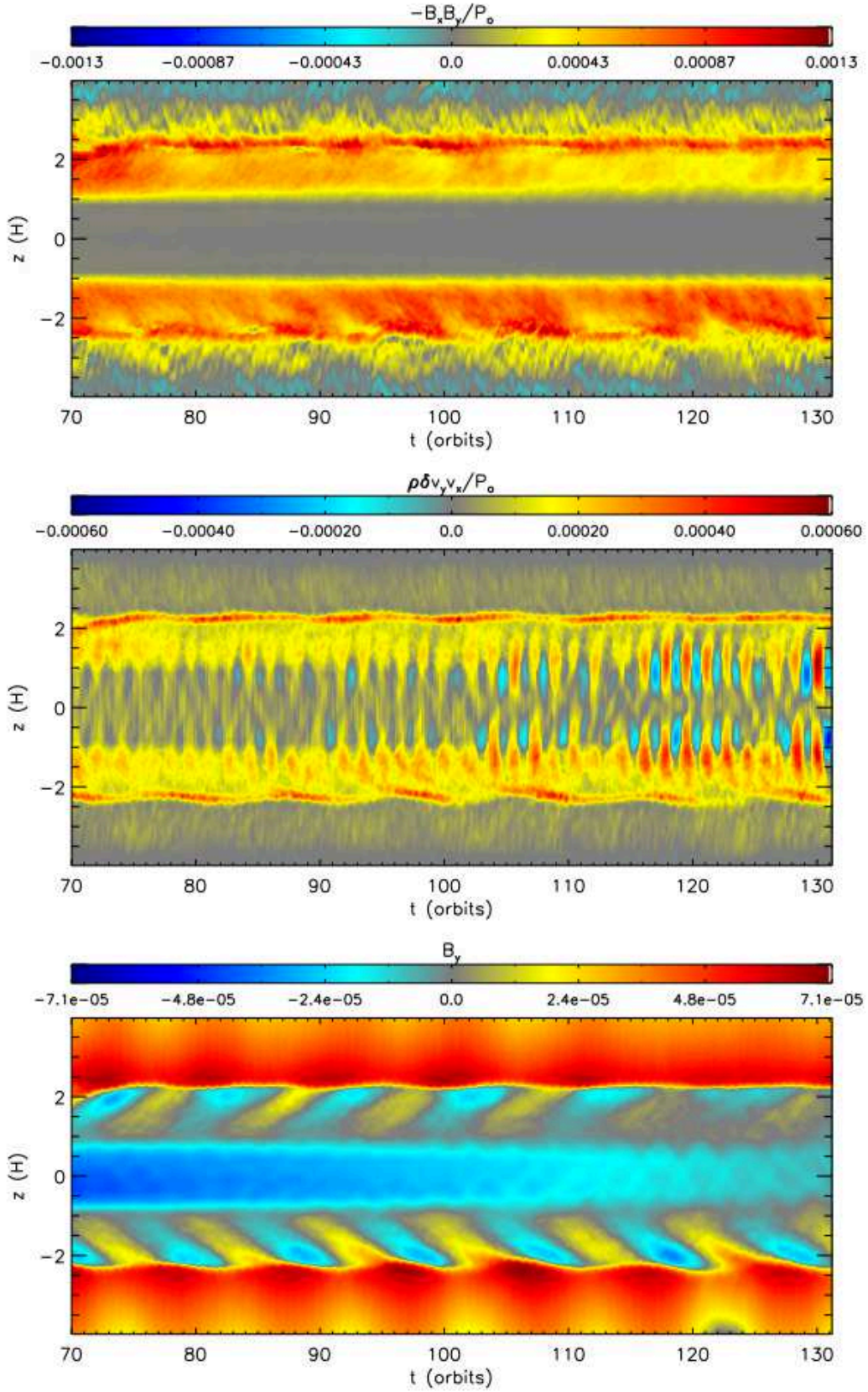


FIG. 10.— Space-time plots of Maxwell stress (top), Reynolds stress (middle) and toroidal field, B_y (bottom) for run Z100AU, where each quantity has been averaged over all x and y . The stresses are normalized by the initial peak gas pressure ($P_o = 5 \times 10^{-7}$), whereas B_y is in code units. There is a clear “active” region between 1 and 2 scale heights above and below the mid-plane, where the Maxwell stress is non-negligible and the toroidal field dynamo is active. Within 1 scale height of the mid-plane, there is no turbulent activity, though there is non-zero Reynolds stress.

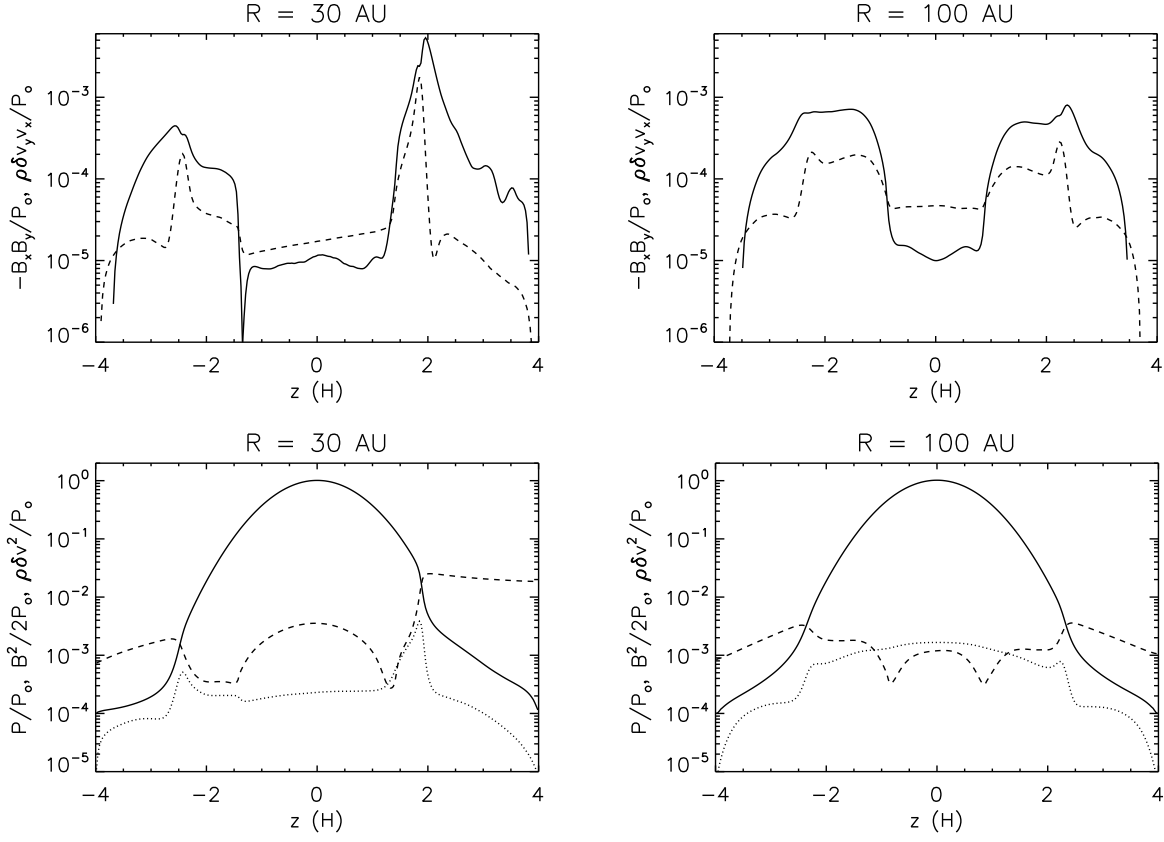


FIG. 11.— Time- and horizontally-averaged stresses (upper row) and energies (bottom row) vs. z in scale heights for the run at 30 AU (left column) and 100 AU (right column). The time average is done from orbit 72 onwards, and the horizontal average is done over all x and y . In the stress plots, the solid line is the Maxwell stress, and the dashed line is the Reynolds stress. In the energy plots, the solid line is the gas pressure, the dashed line is the magnetic energy, and the dotted line is the kinetic energy. All quantities are normalized by the initial peak gas pressure ($P_o = 5 \times 10^{-7}$).

velocity distributions, we have rerun Z30AU with the density floor lowered to 3×10^{-5} (as discussed in Section 3.3). We calculated the velocity distribution for this region during two separate periods, each averaged over 8 orbits. We do not see any significant difference between these velocity distributions and that shown in the middle panel of Fig. 12.

Finally, the rough agreement between turbulent velocity distributions for the vertical velocity and the “in-plane” velocities suggest that turbulent motions will be isotropic, consistent with previous results (Simon et al. 2011a). We point out that velocity distribution for $z > 0$ in Z100AU suggests that the flow is slightly anisotropic. We are not entirely sure why this is the case. However, when we restarted this run and set the turbulent velocity to zero (as described in Section 3.2), the resulting velocity distribution was again nearly isotropic. Since this isotropy is present in all of the other cases, it seems more likely that the distribution for $z > 0$ in Z100AU is a peculiar case, perhaps resulting from the exact nature of the turbulent state from which this run was initiated.

5. SUMMARY AND CONCLUSIONS

We have run local shearing box simulations of MRI-driven turbulence in the presence of ambipolar diffusion and in the absence of a net vertical magnetic field. These simulations were designed to address two primary questions:

- How does MRI-driven turbulence behave in the presence of both ambipolar diffusion and vertical gravity?
- What are the implications for turbulence in the outer regions of protoplanetary disks where ambipolar diffusion is dominant?

With the ambipolar Elsasser number, Am , (see equation 5) remaining constant, we addressed the first question. We found that the density-weighted stress decreases with increasing ambipolar diffusion and decays to negligible values for $Am < 1$. Another parameter that controls the stress levels, however, is the amplitude of the toroidal field strength, which oscillates in time due to the dynamo (Simon et al. 2011b). The stronger the amplitude of oscillation (but not so strong that the MRI is suppressed in the presence of ambipolar diffusion), the larger the turbulent stresses. The average strength of this varying field combined with ambipolar diffusion affect the MRI in such a way that the turbulent stress does not necessarily increase monotonically with decreasing diffusion. All our results are consistent with unstratified numerical simulations of Bai & Stone (2011), although the subtleties of the ambipolar MRI dynamo due to the addition of vertical gravity does not guarantee a one-to-one correspondence between the level of diffusion and that of the turbulent stress.

Additional noticeable effects emerged from these constant Am calculations. First, as ambipolar diffusion is increased, the dynamo oscillation period becomes longer. Above $Am \sim 100$, the oscillation period approaches the ideal MHD limit of 10 orbits. This result opens up more questions than it answers, as we do not yet have an understanding of the dynamo in the ideal MHD limit, let

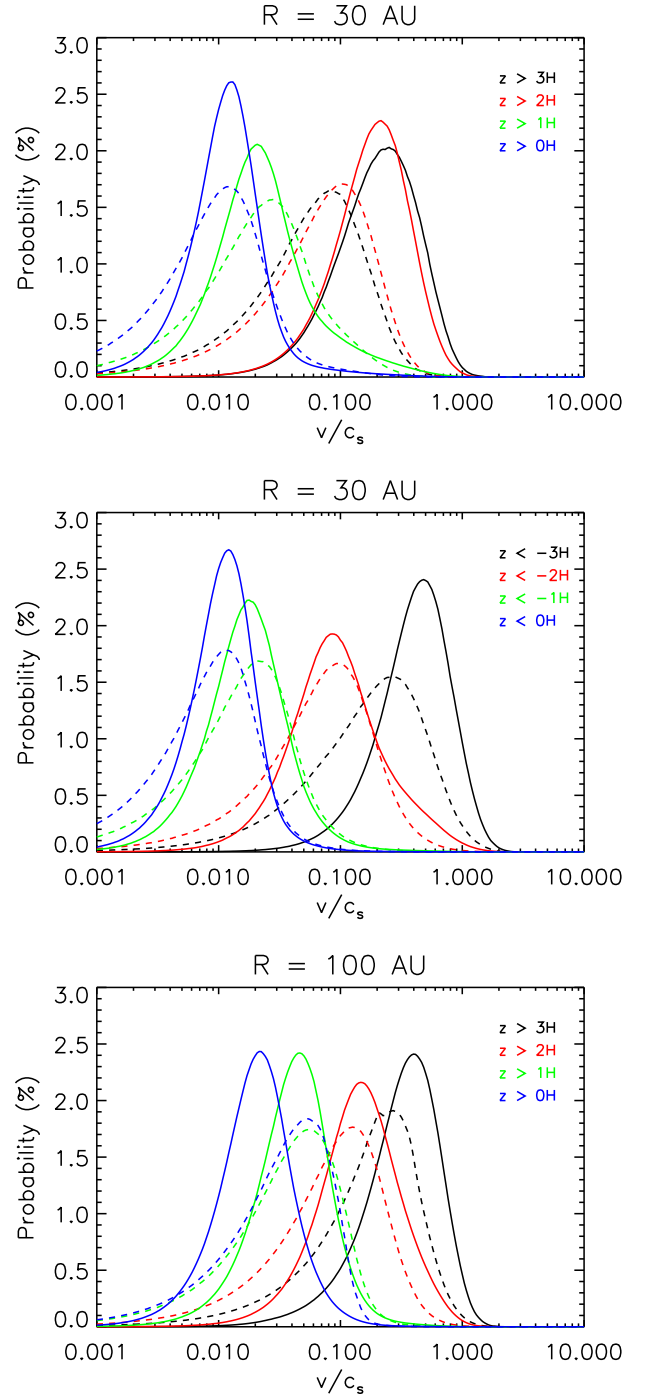


FIG. 12.— Density-weighted turbulent velocity distributions for Z30AU (top and middle) and Z100AU (bottom). The top and bottom panels correspond only to velocities at $z > 0$, whereas the middle panel corresponds to $z < 0$. Each color corresponds to different depths over which the distribution is calculated, as labeled. The dashed lines are the vertical turbulent velocity $|v_z|/c_s$, and the solid lines are the azimuthally averaged disk planar velocity $|v_h|/c_s$. Relatively small velocities exist towards the mid-plane, as turbulence is very weak there. However, far from the mid-plane, the velocity consistently peaks at $v/c_s \sim 0.2 - 0.4$, with part of the distribution going into the supersonic regime.

alone including a diffusion term. However, it may be insightful to apply an ambipolar diffusion term to current, simplified models of the MRI dynamo to help in further understanding the physics of the dynamo. Second, the typical turbulent fluctuations become larger in scale (i.e., have a larger correlation length) and become more aligned with the azimuthal direction as ambipolar diffusion is increased. This last point has important implications for local simulations that include ambipolar diffusion. Increased diffusion evidently favors larger scale fluctuations, and for simulations with strong diffusion, larger shearing boxes are required. A box size of at least $8H \times 16H \times 8H$ is required to properly capture the MRI turbulence with $Am \lesssim 10$. This also motivates further studies of ambipolar diffusion and the MRI in *global simulations*, where one is not limited by scales of order H .

To answer the second of our motivating questions, we ran additional simulations that included a physically motivated model for the ionization structure (and hence Am profile) of the protoplanetary disk. These runs include the effect of a strong FUV ionization layer based upon the work of Perez-Becker & Chiang (2011b), where a large ionization fraction $f \sim 10^{-5}$ can be achieved in a very thin layer above and below the disk mid-plane, while the rest of the disk is assumed to have $Am = 1$. Although this ionization model still bears uncertainties, it provides the essential physical ingredients that allow us to explore the gas dynamics in the outer regions of protoplanetary disks in a realistic manner, again assuming zero vertical magnetic flux.

We find that despite this strong FUV ionization, the mass accretion rate is of order $10^{-9} M_{\odot}/\text{yr}$, too small to account for observed accretion rates measured in T Tauri stars (Gullbring et al. 1998; Hartmann et al. 1998). In fact, this estimate should be treated as an upper limit due to the increase in stress from the relatively large density floor employed. This small accretion rate and the presence of the ambipolar dead zone is reminiscent of models for the Ohmic dead zone (Gammie 1996), many of which also yield low accretion rates. The problem posed by an ambipolar dead zone is, however, more serious. Close to the star, the viscous time scale R^2/ν can be short compared to the disk lifetime given even a weak residual stress. If an Ohmic dead zone can be supplied with gas from further out, it is then possible to imagine gas accumulating there until some additional instability allows gas to flow through on to the star (e.g., Armitage et al. 2001; Zhu et al. 2010; Martin et al. 2012). In the ambipolar dead zone, conversely, low levels of stress imply that the main mass reservoir is permanently inactive. Since this appears to contradict observations, our simulations are either missing some important aspect of the physics, or our basic understanding of disks is incorrect.

There are several possibilities. First, we could be missing some effects that strongly influence the MRI. Including the Hall effect may substantially enhance the strength of MRI turbulence, as indicated by previous works (see the Introduction). Except for the simulations of Sano & Stone (2002a) and Sano & Stone (2002b), no one has carried out non-linear MRI simulations of the Hall effect. Somewhat discouragingly, though, the results of the Sano studies suggest that the Hall effect does not

have a strong influence when Ohmic resistivity is dominant. The same could conceivably be true for ambipolar diffusion dominated regions of the disk as this diffusion acts similar to Ohmic resistivity; it damps out the turbulence.

Alternatively, it is possible that angular momentum transport in the outer disk is dominated by an entirely different physical mechanism, though the known candidates are not expected to be efficient in this region unless the disk mass is high enough that self-gravity is significant (Armitage 2011). It could also be the case that the surface density drops off less rapidly than that assumed in our model. If this is the case, then the induced Reynolds stress from the active layers *may* be able to transport more angular momentum outwards, thus increasing the accretion rate. However, a larger column in the outer disk leads to a smaller active region and thus a smaller induced Reynolds stress. Finally, one cannot exclude the possibility that the disk on 30-100 AU scales is genuinely inviscid, with observed accretion coming from a larger-than-expected reservoir of gas closer to the star.

However, by far the most promising possibility for explaining these low accretion rates is the exclusion of a net vertical magnetic field. Not only is the inclusion of a net vertical field the most optimal magnetic geometry for the MRI with ambipolar diffusion (Bai & Stone 2011), but it is very likely that the disk would be penetrated by at least some amount of vertical field. This vertical field allows the MRI to operate at small values of Am and permits relatively strong turbulence with $\alpha \sim 0.01$ at the mid-plane region of the outer disk (Bai 2011a,b). It should also make the accretion in the FUV ionized layer much more efficient since the vertical field will be relatively strong here due to the drop in gas pressure away from the mid-plane. Indeed, an estimate of the accretion rate based on the models of Perez-Becker & Chiang (2011b) and Bai & Stone (2011) and the simulations of Bai & Stone (2011) (which include the effects of a net vertical magnetic flux) returns a much more optimistic $\dot{M} \sim 10^{-8} M_{\odot}/\text{yr}$. These considerations strongly motivate our companion paper, where we will study in detail the effect of net vertical fields on the accretion process in the limit of strong ambipolar diffusion.

The outer regions of protoplanetary disks can be resolved at sub-mm wavelengths, and with this in mind we have calculated the probability distribution for turbulent velocities as a function of height within the disk. We find that, although the ambipolar dead zone severely restricts the accretion rate, turbulence in the active surface layers remains strong. We obtain peak values of ~ 0.4 of the isothermal sound speed. These results are similar to those found by Simon et al. (2011a) in calculations of Ohmic dead zones at smaller radii, and are consistent with observations of HD 162396 made by Hughes et al. (2011). We predict that the turbulent velocity (and hence line width) ought to be a strong function of height at radii where an ambipolar dead zone is present, which may be testable given observations of multiple molecular tracers that probe different depths within the disk.

The most promising avenue for observational progress lies in ALMA measurements of the spatial structure and velocity field of protoplanetary disks on the same (large) scales as those considered theoretically in this pa-

per. As we have noted, improved measurements of turbulent line broadening (Hughes et al. 2011) at different depths within the disk can potentially provide direct constraints of theoretical models. Such observations appear to be technically feasible (Hughes, private communication). Our results, however, also motivate consideration of disk evolution scenarios that are substantially different from those usually adopted in the interpretation of observational data. It is commonly assumed, for example, that the outer edges of protoplanetary disks expand significantly as the disk evolves viscously. If this is true, then measurements of the disk surface density profile (when fit, for example, by similarity solutions) constrain the radial variation of the angular momentum transport. Our results, on the other hand, suggest that some disks (those with negligible net vertical fields) may not evolve viscously at all on large scales. It may therefore be useful to consider models in which qualitatively different pathways of disk evolution are driven by variations in the initial magnetic flux, rather than by differences in the initial mass and angular momentum content of disk gas. Since strong vertical fields can also lead to angular momentum loss via disk winds (e.g., Salmeron et al. 2011; Lesur et al. 2012), one possible scenario is that strong vertical fields lead to wind-dominated disks, weaker fields to stimulated MRI-driven evolution, and no vertical field to effectively inviscid disks.

We thank Sean O’Neill and John Hawley for useful discussions and suggestions regarding this work. We also thank an anonymous referee for useful comments on an earlier draft of this paper. JBS, PJA, and KB acknowledge support from NASA through grants NNX09AB90G and NNX11AE12G and from the National Science Foundation through grant AST-0807471. KB also acknowledges funding support from Tech-X Corp., Boulder, CO. XB and JMS acknowledge support from the National Science Foundation through grant AST-0908269. XB also acknowledges support for program number HST-HF-51301.01-A provided by NASA through a Hubble Fellowship grant from the Space Telescope Science Institute, which is operated by the Association of Universities for Research in Astronomy, Incorporated, under NASA contract NAS5-26555. This research was supported by an allocation of advanced computing resources provided by the National Science Foundation. The computations were performed on Kraken and Nautilus at the National Institute for Computational Sciences through XSEDE grant TG-AST090106. This work also utilized the Janus supercomputer, which is supported by the National Science Foundation (award number CNS-0821794) and the University of Colorado Boulder. The Janus supercomputer is a joint effort of the University of Colorado Boulder, the University of Colorado Denver, and the National Center for Atmospheric Research.

APPENDIX

SUPER TIME-STEPPING

In this work, we have employed the super time-stepping (STS) technique of Alexiades et al. (1996) to

allow for an accelerated integration while including the effects of strong ambipolar diffusion. Following O’Sullivan & Downes (2006) and O’Sullivan & Downes (2007), the STS method divides a compound timestep Δt_{STS} into N *unequal* substeps $\Delta \tau_j$ ($j = 1, \dots, N$) with

$$\Delta t_{\text{STS}} = \sum_{j=1}^N \Delta \tau_j. \quad (\text{A1})$$

By choosing $\Delta \tau_j$ judiciously, stability can be maintained even when the averaged timestep $\Delta t_{\text{STS}}/N$ is much larger than the normal stable diffusion timestep Δt_{diff} . The optimized lengths for the substeps were found to be (Alexiades et al. 1996; O’Sullivan & Downes 2006, 2007)

$$\Delta \tau_j = \Delta t_{\text{diff}} \left[(\nu - 1) \cos \left(\frac{2j-1}{N} \frac{\pi}{2} \right) + \nu + 1 \right]^{-1}, \quad (\text{A2})$$

where $0 < \nu < 1$ is a free parameter. The sum of the substeps gives

$$\Delta t_{\text{STS}} = \Delta t_{\text{diff}} \frac{N}{2\sqrt{\nu}} \left[\frac{(1 + \sqrt{\nu})^{2N} - (1 - \sqrt{\nu})^{2N}}{(1 + \sqrt{\nu})^{2N} + (1 - \sqrt{\nu})^{2N}} \right] \equiv G(N, \nu) \Delta t_{\text{diff}}. \quad (\text{A3})$$

We note that as $\nu \rightarrow 0$, $\Delta t_{\text{STS}} \rightarrow N^2 \Delta t_{\text{diff}}$ so that the STS approach is asymptotically N times faster than the standard explicit approach. However, the value of ν needs to be properly chosen to achieve the optimal balance between performance and accuracy. In general, the STS method provides better accuracy as N decreases and ν increases, whereas large N and small ν lead to higher efficiency. Here, we choose $\nu = 1/4N^2$ with a limit of $N \leq 12$. At $N = 12$, one achieves an acceleration factor of about 9. It is also found that further increasing N would not significantly increase the efficiency without sacrificing accuracy (Stone, private communication based on a Princeton Junior Project done by Sara Wellons).

In our calculations, we first compute the ideal MHD time step Δt_{MHD} and the diffusion timestep Δt_{diff} . The number of super time steps N can be found from the condition $G[N - 1, 1/4(N - 1)^2] < \Delta t_{\text{MHD}}/\Delta t_{\text{diff}} \leq G(N, 1/4N^2)$. If $N \leq 12$, then we modify Δt_{diff} so that $\Delta t_{\text{MHD}} \equiv G(N, 1/4N^2) \Delta t_{\text{diff}}$. Otherwise, we fix $N = 12$, and set $\Delta t_{\text{MHD}} = \Delta t_{\text{diff}} G[12, 1/(4 \times 12^2)]$. In this way, we always have $\Delta t_{\text{MHD}} = \Delta t_{\text{STS}}$.

As we use an operator-split algorithm for magnetic diffusion, we integrate N STS substeps of the ambipolar diffusion term with $\Delta \tau_j$ before evolving one MHD time step with Δt_{STS} . With STS, we have repeated the test problems (i.e., linear wave damping test and C-type shock test) performed in Bai & Stone (2011) and found essentially the same results for N_{STS} up to 10. Moreover, we repeated the unstratified MRI simulations with $Am = 1$ (runs Z5 and M5 in Bai & Stone (2011)) and with STS turned on. In these simulations N_{STS} reaches 12, and the stress level we find is the same as reported in Bai & Stone (2011). Combining our tests with the successful tests of O’Sullivan & Downes (2006), O’Sullivan & Downes (2007), and Choi et al. (2009), we are confident that the STS technique implemented here is capable of achieving substantial speed-up while maintaining accuracy.

REFERENCES

- Alexiades, V., Amiez, G., & Gremaud, P. 1996, *Communications in Numerical Methods of Engineering*, 12, 31
- Armitage, P. J., Livio, M., & Pringle, J. E. 2001, *MNRAS*, 324, 705
- Armitage, P. J. 2011, *ARA&A*, 49, 195
- Bai, X.-N., & Stone, J. M. 2011, *ApJ*, 736, 144
- Bai, X.-N. 2011, *ApJ*, 739, 50
- Bai, X.-N. 2011, *ApJ*, 739, 51
- Bai, X.-N., & Stone, J. M. 2012, in prep
- Balbus, S. A., & Hawley, J. F. 1998, *Reviews of Modern Physics*, 70, 1
- Balbus, S. A., & Terquem, C. 2001, *ApJ*, 552, 235
- Barge, P., & Sommeria, J. 1995, *A&A*, 295, L1
- Birnstiel, T., Ormel, C. W., & Dullemond, C. P. 2011, *A&A*, 525, 11
- Blaes, O. M., & Balbus, S. A. 1994, *ApJ*, 421, 163
- Brandenburg, A., Nordlund, A., Stein, R. F., & Torkelsson, U. 1995, *ApJ*, 446, 741
- Choi, E., Kim, J., & Wiita, P. J. 2009, *ApJ Supplement*, 181, 413
- Colella, P. 1990, *JCP*, 87, 171
- Colella, P., & Woodward, P. R. 1984, *JCP*, 54, 174
- Davis, S. W., Stone, J. M., & Pessah, M. E. 2010, *ApJ*, 713, 52
- Desch, S. J. 2004, *ApJ*, 608, 509
- Evans, C. R., & Hawley, J. F. 1988, *ApJ*, 332, 659
- Fleming, T., & Stone, J. M. 2003, *ApJ*, 585, 908
- Forgan, D. H.; Armitage, P. J.; & Simon, J. B. 2012, *MNRAS*, in press
- Fromang, S., & Papaloizou, J. 2007, *A&A*, 476, 1113
- Gammie, C. F. 1996, *ApJ*, 457, 355
- Gardiner, T. A., & Stone, J. M. 2005, *JCP*, 205, 509
- . 2008, *JCP*, 227, 4123
- Guan, X., Gammie, C. F., Simon, J. B., & Johnson, B. M. 2009, *ApJ*, 694, 1010
- Gullbring, E., Hartmann, L., Briceno, C., & Calvet, N. 1998, *ApJ*, 492, 323
- Hartmann, L., Calvet, N., Gullbring, E., & D'Alessio, P. 1998, *ApJ*, 495, 385
- Hawley, J. F., Gammie, C. F., & Balbus, S. A. 1995, *ApJ*, 440, 742
- Hawley, J. F., & Stone, J. M. 1998, *ApJ*, 501, 758
- Hayashi, C. 1981, *Progress of Theoretical Physics Supplement*, 70, 35
- Hughes, A. M., Wilner, D. J., Andrews, S. M., Qi, C., & Hogerheijde, M. R. 2011, *ApJ*, 727, 85
- Ida, S., Guillot, T., & Morbidelli, A. 2008, *ApJ*, 686, 1292
- Ilgner, M., & Nelson, R. P. 2006, *A&A*, 445, 205
- Jin, L. 1996, *ApJ*, 457, 798
- Johansen, A., Youdin, A., & Klahr, H. 2009, *ApJ*, 697, 1269
- Kunz, M. W., & Balbus, S. A. 2004, *MNRAS*, 348, 355
- Lesur, G., Ferreira, J., & Ogilvie, G. 2012, *arXiv:1210.6660*
- Low, M.-M. M., Norman, M. L., Konigl, A., & Wardle, M. 1995, *ApJ*, 442, 726
- Martin, R. G., Lubow, S. H., Livio, M., & Pringle, J. E. 2012, *MNRAS*, 423, 2718
- Mignone, A. 2007, *JCP*, 225, 1427
- Miyoshi, T., & Kusano, K. 2005, *JCP*, 208, 315
- Najita, J. R., Strom, S. E., & Muzerolle, J. 2007, *MNRAS*, 378, 369
- Oishi, J. S., & Low, M.-M. M. 2009, *ApJ*, 704, 1239
- Ormel, C. W., & Cuzzi, J. N. 2007, *A&A*, 466, 413
- O'Sullivan, S., & Downes, T. P. 2006, *MNRAS*, 366, 1329
- . 2007, *MNRAS*, 376, 1648
- Paardekooper, S. J., Baruteau, C., & Kley, W. 2011, *MNRAS*, 410, 293
- Perez-Becker, D., & Chiang, E. 2011, *ApJ*, 727, 2
- Perez-Becker, D., & Chiang, E. 2011, *ApJ*, 735, 8
- Salmeron, R., Königl, A., & Wardle, M. 2011, *MNRAS*, 412, 1162
- Sano, T., & Stone, J. M. 2002a, *ApJ*, 570, 314
- . 2002b, *ApJ*, 577, 534
- Shakura, N. I., & Syunyaev, R. A. 1973, *A&A*, 24, 337
- Sicilia-Aguilar, A., Henning, T., & Hartmann, L. W. 2010, *ApJ*, 710, 597
- Simon, J. B., Armitage, P. J., & Beckwith, K. 2011a, *ApJ*, 743, 17
- Simon, J. B., Beckwith, K., & Armitage, P. J. 2012, *MNRAS*, 422, 2685
- Simon, J. B., Hawley, J. F., & Beckwith, K. 2011b, *ApJ*, 730, 94
- Sorathia, K. A., Reynolds, C. S., Stone, J. M., & Beckwith, K. 2012, *ApJ*, 749, 189
- Stone, J. M., Hawley, J. F., Gammie, C. F., & Balbus, S. A. 1996, *ApJ*, 463, 656
- Stone, J. M., & Gardiner, T. A. 2010, *ApJS*, 189, 142
- Stone, J. M., Gardiner, T. A., Teuben, P., Hawley, J. F., & Simon, J. B. 2008, *ApJS*, 178, 137
- Turner, N. J., & Sano, T. 2008, *ApJ*, 679, L131
- Turner, N. J., Sano, T., & Dziourkevitch, N. 2007, *ApJ*, 659, 729
- Uribe, A. L., Klahr, H., Flock, M., & Henning, T. 2011, *ApJ*, 736, 85
- Wardle, M. 1999, *MNRAS*, 307, 849
- Wardle, M., & Salmeron, R. 2012, *MNRAS*, 422, 2737
- Weidenschilling, S. J. 1977, *Ap&SS*, 51, 153
- Youdin, A. N., & Lithwick, Y. 2007, *Icarus*, 192, 588
- Zhu, Z., Hartmann, L., Gammie, C. F., et al. 2010, *ApJ*, 713, 1134